

Journal of Biomedical Optics

BiomedicalOptics.SPIEDigitalLibrary.org

Photoacoustic microscopy of arteriovenous shunts and blood diffusion in early-stage tumors

Chenghung Yeh
Jinyang Liang
Yong Zhou
Song Hu
Rebecca E. Sohn
Jeffrey M. Arbeit
Lihong V. Wang

SPIE.

Photoacoustic microscopy of arteriovenous shunts and blood diffusion in early-stage tumors

Chenghung Yeh,^a Jinyang Liang,^b Yong Zhou,^b Song Hu,^c Rebecca E. Sohn,^d Jeffrey M. Arbeit,^{d,*} and Lihong V. Wang^{a,b,*}

^aWashington University in St. Louis, Department of Electrical and Systems Engineering, One Brookings Drive, St. Louis, Missouri 63130, United States

^bWashington University in St. Louis, Department of Biomedical Engineering, One Brookings Drive, St. Louis, Missouri 63130, United States

^cUniversity of Virginia, Department of Biomedical Engineering, PO Box 800759, Charlottesville, Virginia 22908, United States

^dWashington University School of Medicine, Department of Surgery, Urology Division, St. Louis, Missouri 63130, United States

Abstract. Angiogenesis in a tumor region creates arteriovenous (AV) shunts that cause an abnormal venous blood oxygen saturation (sO_2) distribution. Here, we applied optical-resolution photoacoustic microscopy to study the AV shunting *in vivo*. First, we built a phantom to image sO_2 distribution in a vessel containing converged flows from two upstream blood vessels with different sO_2 values. The phantom experiment showed that the blood from the two upstream vessels maintained a clear sO_2 boundary for hundreds of seconds, which is consistent with our theoretical analysis using a diffusion model. Next, we xenotransplanted O-786 tumor cells in mouse ears and observed abnormal sO_2 distribution in the downstream vein from the AV shunts *in vivo*. Finally, we identified the tumor location by tracing the sO_2 distribution. Our study suggests that abnormal sO_2 distribution induced by the AV shunts in the vessel network may be used as a new functional benchmark for early tumor detection. © 2016 Society of Photo-Optical Instrumentation Engineers (SPIE) [DOI: 10.1117/1.JBO.21.2.020501]

Keywords: optical-resolution photoacoustic microscopy; arteriovenous shunt effect; hemoglobin oxygen saturation; angiogenesis; Fick's law of diffusion.

Paper 150804LRR received Dec. 1, 2015; accepted for publication Jan. 21, 2016; published online Feb. 16, 2016.

In the cardiovascular system, arteries transport red blood cells (RBCs) containing oxygenated hemoglobin to capillaries, where oxygen is extracted to cells. Next, the oxygen-unloaded RBCs flow to veins. In a healthy circulation system, the concentration of oxygenated hemoglobin in arteries is much higher than that in veins and is reflected in a higher value of oxygen saturation of hemoglobin (sO_2). In contrast, as a cancerous tumor grows in tissue, angiogenesis causes vessel remodeling to supply the

tumor tissue with oxygen and nutrition.¹ This process may lead to the development of arteriovenous (AV) shunts—abnormal vessels that directly connect arteries with veins. In the tumor microvasculature, AV shunts result in high sO_2 in veins. The resultant dysfunctional microcirculation² alters the drug delivery efficiency.³ Recently, controlling tumor growth by normalizing the tumor circulation has attracted increasing interests, either by using antiangiogenic drugs alone⁴ or by combining antiangiogenic drugs and chemotherapy.³ However, early detection of the AV shunt effect in tumor development remains a challenge.

The AV shunt effect has been studied with several imaging modalities.^{5–11} For example, intravital microscopy (IVM) has been used to quantify the hemodynamic changes in the AV shunt.^{7,11} However, IVM is invasive because it generally requires surgical preparation to observe capillaries. Other imaging modalities, such as large-field gamma imaging, sidestream dark-field imaging, x-ray imaging, and two-photon microscopy, have been adopted for studying the effect.^{5–10} However, these techniques either lack sufficient spatial resolution or need exogenous contrast agents. More importantly, none of the techniques mentioned above can detect AV shunting by monitoring sO_2 .

In comparison, optical-resolution photoacoustic microscopy (OR-PAM)^{12,13} can overcome the above limitations. OR-PAM uses endogenous optical absorption contrast to achieve label-free, high-resolution, noninvasive imaging of microvasculature.^{14,15} In addition to structural imaging, OR-PAM also enables measuring functional hemodynamic parameters including the concentration of hemoglobin and sO_2 ,¹⁴ blood flow velocity,^{16,17} and the metabolic rate of oxygen.¹⁴ Moreover, OR-PAM has been applied to the study of metabolism in tumors and has demonstrated its capability to longitudinally monitor tumor growth.^{14,18} However, so far, the AV shunt effect has not been studied by OR-PAM in detail.

In this letter, we hypothesize that the AV shunt effect can be detected downstream of a tumor by its abnormal sO_2 value. Specifically, we are interested in the spatial and temporal distributions of sO_2 in veins draining from normal and abnormal regions. To validate our hypothesis, we first conducted a phantom experiment to study the sO_2 spatial distribution due to both oxygen and hemoglobin diffusions. Then we investigated confluence vessels in a tumor *in vivo*. By imaging the AV shunts, we can trace the abnormal vessel back to the tumor.

Our OR-PAM system (Fig. 1) uses a nanosecond-pulsed solid-state laser (INNOSLAB, Edgewave, 532- and 559-nm wavelengths; 30-kHz pulse repetition rate).¹⁹ The laser beam first passes through an iris (ID25SS, Thorlabs; 2-mm aperture). Then a spatial filtering stage consisting of a condenser lens (LA1131, Thorlabs) and a pinhole (P50C, Thorlabs) filters the laser beam. The spatially filtered beam is coupled into a single-mode photonic crystal fiber (LMA-10, NKT Photonics) by an objective lens (4 \times , NA = 0.1, Leica). A beam sampler (BSF10-A, Thorlabs) and a homemade photodiode detector are placed before the fiber to monitor the laser intensity fluctuation. The output beam from the fiber is collimated by an objective lens (RMS4 \times , Thorlabs) and then focused by another identical objective lens onto the target. The theoretical diffraction-limited optical focal diameter is 2 μ m. The sample absorbs the nanosecond pulse, which induces a local temperature rise. Subsequently, the increased temperature results in thermoelastic expansion that generates photoacoustic waves.

*Address all correspondence to: Jeffrey M. Arbeit, E-mail: arbeitj@wustl.edu; Lihong V. Wang, E-mail: lhwang@wustl.edu

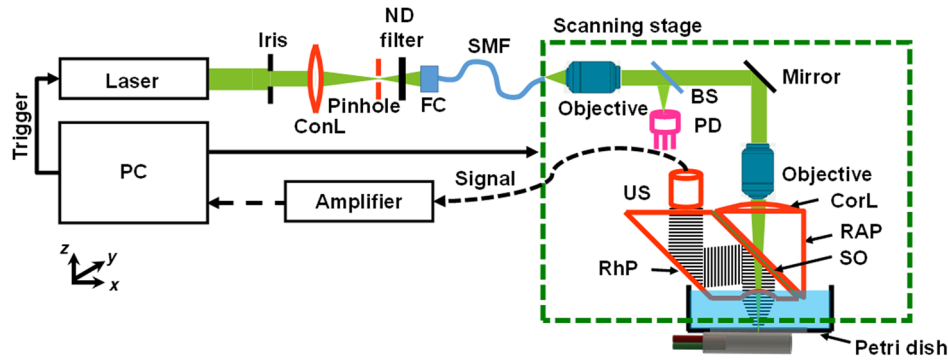


Fig. 1 Schematic of OR-PAM. BS, beam splitter; ConL, condenser lens; CorL, correction lens; FC, fiber coupler; ND, neutral density; PD, photodiode; RAP, right-angle prism; RhP, rhomboid prism; SMF, single-mode fiber; SO, silicone oil; and US, ultrasonic transducer.

The photoacoustic waves are reflected by an intervening layer of silicone oil between two prisms (Fig. 1) and then detected by an ultrasonic transducer (V214-BB-RM, Olympus-NDT). The detected photoacoustic signal is amplified by two electrical amplifiers in series (ZFL 500LN and Mini-Circuits) followed by digitization (ATS9350, Alazar Tech Inc.).

To simulate the sO_2 distribution at the confluence of an abnormal vein and a normal vein, we made a polycarbonate bifurcation tube phantom [Fig. 2(a)], which consisted of two identical smaller-diameter tubes (ID $187.5 \mu\text{m}$, OD $250 \mu\text{m}$;

CTPC187-250, Paradigm Optics) and a larger-diameter tube (ID $500 \mu\text{m}$, OD $750 \mu\text{m}$; CTPC500-750, Paradigm Optics) to model the upstream daughter veins and the downstream parent vein, respectively. The junction of the three tubes was sealed by glue. The other ends of the two smaller-diameter tubes were connected to two individual syringes, each driven by a syringe pump (NE-300, Pump Systems, Inc.). We used blood with high sO_2 (0.90) and low sO_2 (0.54) in the two smaller-diameter tubes, from where the blood was pumped into the confluence tube.

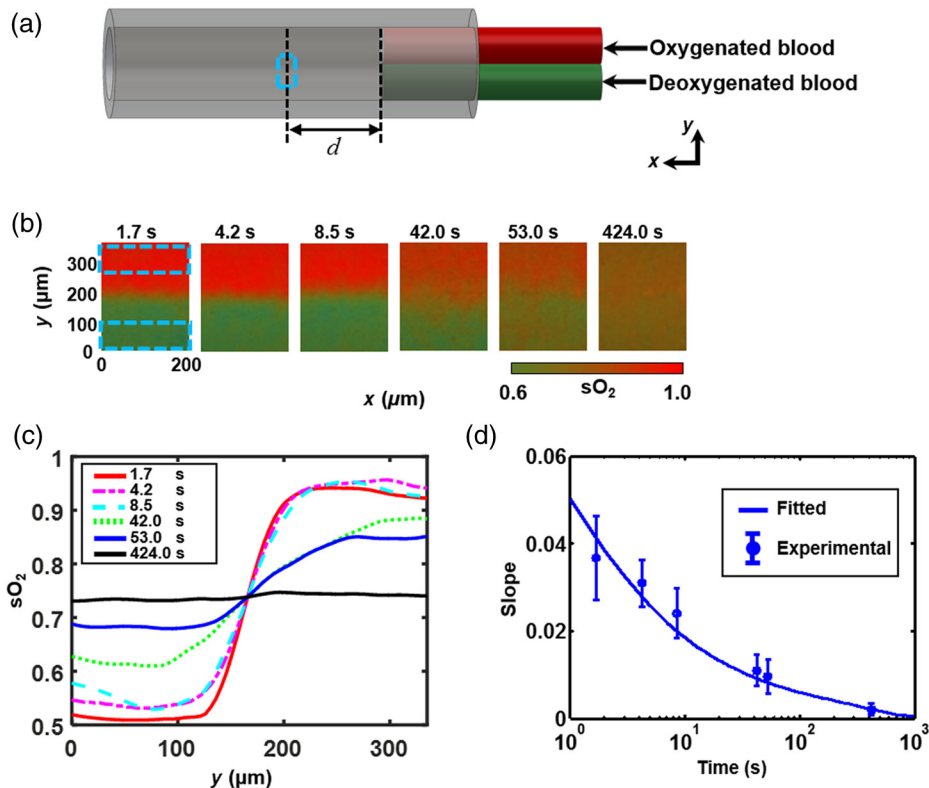


Fig. 2 OR-PAM of AV shunt effect in phantom. (a) Schematic of phantom. Two smaller-diameter tubes (ID $187.5 \mu\text{m}$, OD $250 \mu\text{m}$) are inserted into one larger-diameter tube (ID $500 \mu\text{m}$, OD $750 \mu\text{m}$). One small tube was injected with oxygenated blood and the other with deoxygenated blood. The blood flow was controlled by a syringe pump for each small tube. The dashed box indicates the imaging region of interest. (b) Measured sO_2 distributions at equivalent time points of 1.7, 4.2, 8.5, 42.0, 53.0, and 424.0 s. (c) sO_2 averaged along x versus y at equivalent time points of 1.7, 4.2, 8.5, 42.0, 53.0, and 424.0 s. (d) Measured sO_2 slopes along the y direction at the center of the tube versus time and fit based on a diffusion model.

Given the blood flow speed, we can potentially obtain the time course of the sO_2 distribution by scanning a large region of the confluence vessel. However, the limited field of view ($20 \times 20 \text{ mm}^2$) of the OR-PAM system imposes a limited time window. Instead, we varied the upstream blood flow speed (v) from 7.1×10^{-3} to 1.8 mm/s and scanned an area of interest on the tube [$2.5 \mu\text{m} \times 5.0 \mu\text{m}$ step size; $200 \times 365 \mu\text{m}^2$ image size, marked by the dashed box in Fig. 2(a)], located at a constant distance ($d = 3 \text{ mm}$) from the confluence point. This approach allowed us to obtain the sO_2 distribution at various effective time points ($t = d/v$) spread over a sufficiently large range. The experimental results at multiple time points (1.7, 4.2, 8.5, 42.0, 53.0, and 424.0 s) are shown in Fig. 2(b).

To analytically study the sO_2 distribution along the cross section of the confluence vessel [the y -axis in Fig. 2(a)], we established a simple model based on Fick's law of diffusion:^{20,21}

$$J = -D_{\text{eff}} \frac{\partial [O_2]_{\text{bound}}}{\partial y}, \quad (1)$$

where J , D_{eff} , and $[O_2]_{\text{bound}}$ denote the total flux of oxygen along the y -axis, the effective oxygen diffusion coefficient, and bound oxygen concentration, respectively. Here, we assume that sO_2 diffusion is governed by both free oxygen diffusion and RBC diffusion.²² The effective diffusion coefficient can be approximately estimated by

$$D_{\text{eff}} \approx D_{\text{RBC}} + \frac{\alpha \times \beta'}{[O_2]_{\text{bound-max}}} \times D_{\text{oxygen}}, \quad (2)$$

where α , β' , and $[O_2]_{\text{bound-max}}$, respectively, denote the solubility of oxygen, the slope of the quasilinear portion of the oxygen dissociation curve (i.e., the portion between P_{43} and P_{91}), and the maximum concentration of oxygen carried by RBCs. Based on the thin-film solution,²³ the sO_2 distribution $c(y, t)$ along the cross section of the confluence vessel can be expressed as

$$c(y, t) = \frac{1}{\sqrt{4\pi D_{\text{eff}} t}} \int_0^l c(y', 0) \exp\left[-\frac{(y - y')^2}{4D_{\text{eff}} t}\right] dy', \quad (3)$$

where l denotes the diameter of the tube.

The measured sO_2 values at each time point [Fig. 2(b)] were averaged along the x -axis [Fig. 2(c)]. Then we chose the maximum slope of each sO_2 curve with respect to y to quantify the diffusion speed, to which the flux of oxygen is proportional according to Eq. (1). As shown in Fig. 2(d), the PAM-measured sO_2 slopes were fitted with an effective diffusion coefficient ($D_{\text{eff}} = 7.5 \times 10^{-7} \text{ cm}^2/\text{s}$) according to Eq. (3). The fitted effective diffusion coefficient is larger than the RBC diffusion coefficient ($D_{\text{RBC}} = 4 \times 10^{-7} \text{ cm}^2/\text{s}$) but smaller than the free oxygen diffusion coefficient ($D_{\text{oxygen}} = 1.5 \times 10^{-5} \text{ cm}^2/\text{s}$) reported in the literature.^{22,24} This observation is likely due to that most oxygen (98.5%) is carried by RBCs, and only a small amount of free oxygen (1.5%) is dissolved in the blood. From Eq. (2), we obtain $D_{\text{eff}} \approx 8.0 \times 10^{-7} \text{ cm}^2/\text{s}$, which is comparable with the fitted value. These results predict that when the initial sO_2 concentration difference is 0.36, a distinguishable sO_2 boundary can persist for $\sim 100 \text{ s}$ in a $100\text{-}\mu\text{m}$ -diameter vessel. Note that the sO_2 boundary corresponded to the point with the maximum slope with respect to y of each averaged sO_2 curve in Fig. 2(b). Moreover, the noise level was quantified by averaging the standard deviations over the undiffused high sO_2 and low sO_2 areas [dashed boxes in

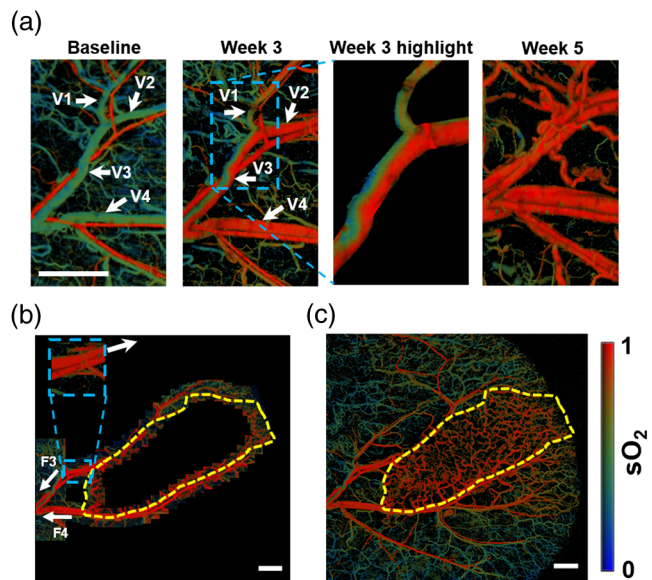


Fig. 3 OR-PAM of AV shunt effect in a mouse ear *in vivo*. (a) sO_2 images of a mouse ear acquired before (baseline), 3 weeks after, and 5 weeks after injection of the xenotransplanted O-786 cells. The blue dashed box encloses a highlighted region. V1, normal vessel; V2, week 3 abnormal vessel; V3, confluence vessel of V1 and V2; and V4, week 3 high sO_2 vein. (b) Tiled image of the sO_2 map in a mouse ear using a 3-D arbitrary trajectory scan (the corresponding movie is Video 1). The yellow dashed line bounds the predicted tumor region. F3 and F4, flow directions of veins V3 and V4. (c) Whole-ear sO_2 map imaged by raster scan. The yellow dashed line region encloses the tumor region. Scale bars = 1 mm. (Video 1, MOV, 237 kb) [URL: <http://dx.doi.org/10.1117/1.JBO.21.2.020501.1>].

Fig. 2(b)]. The sO_2 boundary is considered distinguishable if the difference in sO_2 between these two areas is three times greater than the noise level. As the normal venous blood flow speed in mice is 5 mm/s ,¹⁴ this sO_2 boundary should be able to last for as long as 500 mm .

To study the AV shunt effect *in vivo*, we imaged O-786 xenograft tumor in the mouse ear. The Animal Studies Committee of Washington University in St. Louis approved all animal care and experimental procedures. OR-PAM imaged the sO_2 distribution of four mice, once per week for 6 weeks. All of them showed similar sO_2 landscapes. As an example, Fig. 3 presents the sO_2 map of a mouse ear at three different time points: the baseline before, 3 weeks after, and 5 weeks after tumor xenograft. First, we monitored the region enclosing the first bifurcation of the main vessel pair. For the baseline image, our measured sO_2 values at the trunk vessel region in a healthy mouse ear were ~ 0.90 for arteries and ~ 0.55 for veins [Fig. 3(a), left], which agreed well with the literature.¹⁴ At week 3, an abnormal sO_2 distribution was found, and portions of the veins expressed much higher sO_2 values than expected [Fig. 3(a), middle]. Finally, the tumor at week 5 was fully established and affected the whole imaged region [Fig. 3(a), right]. In addition, the flow speed and diameter of the confluence vein (V3) were quantified to be 5 mm/s and $180 \mu\text{m}$, respectively. According to Eq. (2), it should take 185 s for the high sO_2 and low sO_2 blood to mix in the confluence vessel, corresponding to $\sim 900\text{-mm}$ distance at the given blood flow speed. In the week 3 image [Fig. 3(a), middle], the sO_2 in vein V2 has a higher value than that for the baseline image. The abnormally high sO_2 vein values were caused by an AV shunt. As a result, blood entering the confluence vessel (V3) was drained from one normal vein

(V1) and one abnormal vein (V2). By analyzing the sO_2 distribution, we found a clear sO_2 boundary in the confluence vein (V3), and this sO_2 boundary was maintained in the entire imaged vessel (~ 1.5 -mm long).

These measurements uncovered a new way to detect abnormal vessels in the shunted region—detecting the boundary at a spot far away from the tumor region and tracing these vessels back to the tumor region. To verify our approach, we first performed a raster scan and imaged a small region (~ 1.25 mm \times 4.00 mm) of the trunk vessel. We identified the abnormal trunk vessels (V3 and V4) at week 3 in Fig. 3(a) and marked the direction of these blood flows (F3 and F4) in Fig. 3(b). Then we implemented a three-dimensional (3-D) arbitrary trajectory scan,¹⁹ which allowed 3-D position adjustment to trace the targeted vessels. By tracing these abnormal vessels against the flow direction to the bifurcation point, we identified the healthy region and the abnormal region based on sO_2 values: the threshold sO_2 value for an abnormal vein is defined as the mean of the values for a normal artery and vein. Next, we moved the scanning region by a small step (0.35 mm) based on the tangential direction of the targeted vessel in the abnormal region and repeated the procedures above. Here, the tangential direction of the vessel is calculated from the segment on the vein at the upstream side of the small window [inset in Fig. 3(b)]. Finally, all images were stitched together to form Fig. 3(b), and a corresponding movie is provided in Video 1. Based on the trace, we predicted the tumor region (yellow dashed circle) by enclosing the region with an abnormal sO_2 value. To validate our prediction, we performed a whole ear raster scan [Fig. 3(c)] to identify the tumor region [yellow dashed circle in Fig. 3(c)], which is distinguished by vessels with abnormally high sO_2 values and high density.¹⁴ By comparing with Fig. 3(b), we confirmed that the predicted tumor region agreed well with the tumor region. Here, the unique hemodynamic characteristic of the AV shunt, plus the low diffusion rate of hemoglobin, suggests that sO_2 -based tracking can potentially be used as a new technique for early tumor detection.

In summary, functional OR-PAM can noninvasively provide sO_2 information with high spatial resolution and detect the AV shunt effect by mapping the sO_2 distribution of a confluence vein near an early tumor region. The theoretical study and phantom experiments showed that the sO_2 boundary induced by the AV shunt can persist for around 900 μ m at the vessel parameters in the *in vivo* experiments. By using the sO_2 distribution, we successfully traced an early tumor in a mouse ear *in vivo*. Our study suggests that the abnormal sO_2 distribution induced by the AV shunt can potentially be used as a functional technique for early cancer detection. In the future, the penetration depth of functional OR-PAM can be improved by using near-infrared light for excitation, which is more weakly optically scattered than visible light.²⁵ We also plan to apply our approach with photoacoustic computed tomography (PACT), which has a penetration depth of up to 8 cm.¹² Although it is difficult to compensate for the unknown local fluence in PACT, a calibration-free method can be employed to achieve absolute sO_2 measurement.²⁶ By exploiting the ability to image the shunt effect, which identifies an abnormal vessel and its source, we may be able to trace early tumor growth in humans.

Acknowledgments

The authors appreciate the close reading of the manuscript by Professor James Ballard. We also thank Cheng Ma, Pengfei Hai,

and Hsun-Chia Hsu for helpful discussions. This work was sponsored by the National Institutes of Health under Grants DP1 EB016986 (NIH Director's Pioneer Award), R01 CA186567 (NIH Director's Transformative Research Award), and R01 CA159959. Competing financial interests: L.V.W. has financial interests in Microphotoacoustics, Inc. and Endra, Inc., neither of which supported this work.

References

1. A. Birbrair et al., "Type-2 pericytes participate in normal and tumoral angiogenesis," *Am. J. Physiol.: Cell Physiol.* **307**(1), C25–C38 (2014).
2. A. R. Pries et al., "The shunt problem: control of functional shunting in normal and tumour vasculature," *Nat. Rev. Cancer* **10**, 587 (2010).
3. R. K. Jain, "Normalization of tumor vasculature: an emerging concept in antiangiogenic therapy," *Science* **307**(5706), 58 (2005).
4. R. K. Jain, "Lessons from multidisciplinary translational trials on anti-angiogenic therapy of cancer," *Nat. Rev. Cancer* **8**, 309 (2008).
5. R. H. Wheeler et al., "Tumor blood flow and systemic shunting in patients receiving intraarterial chemotherapy for head and neck cancer," *Cancer Res.* **46**(8), 4200 (1986).
6. C. Ince, "The microcirculation is the motor of sepsis," *Crit. Care* **9**(4), S13 (2005).
7. M. Lauterbach et al., "Shunting of the microcirculation after mesenteric ischemia and reperfusion is a function of ischemia time and increases mortality," *Microcirculation* **13**(5), 411 (2006).
8. L. An, J. Qin, and R. K. Wang, "Ultrasound sensitive optical microangiography for *in vivo* imaging of microcirculations within human skin tissue beds," *Opt. Express* **18**(8), 8220 (2010).
9. A. Y. Shih et al., "Two-photon microscopy as a tool to study blood flow and neurovascular coupling in the rodent brain," *J. Cereb. Blood Flow Metab.* **32**(7), 1277 (2012).
10. R. L. de Saunders and M. A. Bell, "X-ray microscopy and histochemistry of the human cerebral blood vessels," *J. Neurosurg.* **35**(2), 128 (1971).
11. S. Brem, R. Cotran, and J. Folkman, "Tumor angiogenesis: a quantitative method for histologic grading," *J. Natl. Cancer Inst.* **48**, 347 (1972).
12. L. V. Wang and S. Hu, "Photoacoustic tomography: *in vivo* imaging from organelles to organs," *Science* **335**(6075), 1458 (2012).
13. J. Liang et al., "Spatially Fourier-encoded photoacoustic microscopy using a digital micromirror device," *Opt. Lett.* **39**(3), 430 (2014).
14. J. Yao et al., "Label-free oxygen-metabolic photoacoustic microscopy *in vivo*," *J. Biomed. Opt.* **16**(7), 076003 (2011).
15. C. Yeh et al., "Photoacoustic microscopy of blood pulse wave," *J. Biomed. Opt.* **17**(7), 070504 (2012).
16. Y. Zhou et al., "Calibration-free *in vivo* transverse blood flowmetry based on cross correlation of slow time profiles from photoacoustic microscopy," *Opt. Lett.* **38**(19), 3882 (2013).
17. B. Ning et al., "Simultaneous photoacoustic microscopy of microvascular anatomy, oxygen saturation, and blood flow," *Opt. Lett.* **40**(6), 910 (2015).
18. C. Yeh et al., "Optical-resolution photoacoustic microscopy of the metabolic rate of oxygen in a mouse renal tumor model," *Proc. SPIE* **9323**, 93233H (2015).
19. C. Yeh et al., "Three-dimensional arbitrary trajectory scanning photoacoustic microscopy," *J. Biophotonics* **8**(4), 303 (2014).
20. E. L. Cussler, *Diffusion: Mass Transfer in Fluid Systems*, Cambridge University Press, Cambridge, United Kingdom (2009).
21. D. E. Laughlin et al., *Polycrystalline Metal and Magnetic Thin Films*, MRS Proceedings, Vol. 562 (1999).
22. R. N. Pittman, *Colloquium Series on Integrated Systems Physiology: From Molecule to Function*, Vol. 3, pp. 1–100, Morgan & Claypool Life Sciences, San Rafael, California (2011).
23. P. F. Green, *Kinetics, Transport, and Structure in Hard and Soft Materials*, CRC Press, Boca Raton, Florida (2005).
24. L. R. Adams and I. Fatt, "The diffusion coefficient of human hemoglobin at high concentrations," *Respir. Physiol.* **2**(3), 293 (1967).
25. P. Hai et al., "Near-infrared optical-resolution photoacoustic microscopy," *Opt. Lett.* **39**(17), 5192 (2014).
26. J. Xia et al., "Calibration-free quantification of absolute oxygen saturation based on the dynamics of photoacoustic signals," *Opt. Lett.* **38**(15), 2800 (2013).